

1 **Constraining the aggradation mode of Pleistocene river**
2 **deposits based on cosmogenic radionuclide depth profiling and**
3 **numerical modelling.**

4
5 **Nathan Vandermaelen¹, Koen Beerten², François Clapuyt^{1,3}, Marcus Christl⁴, Veerle**
6 **Vanacker¹**

7 ¹Georges Lemaître Centre for Earth and Climate Research, Earth and Life Institute, UCLouvain, Place Louis
8 Pasteur 3, 1348 Louvain-la-Neuve, Belgium

9 ²Engineered and Geosystems Analysis, Waste and Disposal, Belgian Nuclear Research Centre SCK•CEN,
10 Boeretang 200, 2400 Mol, Belgium

11 ³Fonds de la Recherche Scientifique FRS-FNRS, Brussels, Belgium

12 ⁴Laboratory of Ion Beam Physics, ETH Zurich, Department of Physics, Zurich, Switzerland

13

14 *Correspondence to:* nathan.vandermaelen@uclouvain.be, veerle.vanacker@uclouvain.be

15

16 **Abstract.** Pleistocene braided river deposits commonly represent long periods of non-deposition or erosion that
17 are interrupted by rapid and short aggradation phases. When dating these sedimentary sequences with **in situ**
18 produced cosmic radionuclides (CRN), simple concentration-depth profiling approaches fall often short as they
19 assume that the alluvial sedimentary sequence has been deposited with a constant and rapid aggradation rate and
20 been exposed to cosmic radiations afterwards. Numerical modelling of the evolution of CRNs in alluvial
21 sequences permits to account for aggradation, non-deposition and erosion phases, and can simulate which
22 scenarios of aggradation and preservation are most likely representing the river dynamics. In this study, such a
23 model was developed and applied to a Middle Pleistocene gravel sheet (Zutendaal gravels) exposed in NE
24 Belgium. The model parameters were optimized to the observed ¹⁰Be and ²⁶Al concentrations of 17 sediment

25 samples taken over a depth interval of 7 m that constitutes the top of a gravel sheet up to 20 m thick. In the
26 studied sedimentary sequence, (at least) three individual aggradation phases can be distinguished that were
27 interrupted by non-deposition or erosion, each interruption lasting ~40 kyr. The age for the onset of aggradation
28 of the upper 7 m of the gravel sheet was further constrained to 654^{+218}_{-62} ka. This age, within error limits, does not
29 invalidate previous correlations of the gravel sheet with the Cromerian Glacial B, and marine isotope stage
30 (MIS) 16. The deposition of the entire gravel sheet likely represents more than one climatic cycle, and
31 demonstrates the importance of accounting for the depositional modes of braided rivers when applying in situ
32 cosmogenic radionuclide techniques.

33

34 **Keywords:** Fluvial deposits, Quaternary, erosion, depositional age, ^{10}Be , ^{26}Al , braided river, age-depth.

35

36 1 Introduction

37 In situ produced cosmogenic radionuclides (CRNs, e.g. ^{10}Be and ^{26}Al) are now widely used to infer erosion rates
38 and exposure time of depositional landforms, and allow to better constrain the long-term landscape evolution of
39 the Quaternary (e.g., Hancock et al., 1999; Schaller et al., 2001; Hidy et al., 2018). To constrain the post-
40 depositional history of fluvial deposits, depth profiles are often used. They consist in measuring the CRN
41 concentration over a depth interval of several meters below the surface. The CRN concentration in the upper 2 to
42 3 m decreases exponentially with depth, and the shape of the CRN depth profile informs on the average erosion
43 rate and the post-depositional age. Below 3 m, the CRN concentration asymptotically decreases to a value that is
44 assumed to represent the CRNs conserved from previous exposure episodes, the pre-depositional inheritance (e.g.,
45 Siame et al., 2004; Braucher et al., 2009; Hidy et al., 2010).

46 Measured CRN concentrations can then be fitted to numerical model predictions via an optimization process. A
47 minimum of 5 samples from the same, undisturbed sedimentary sequence is often necessary to obtain reliable
48 results for exposure and erosion rates (Braucher et al., 2009; Hidy et al., 2010; Laloy et al., 2017). The depth
49 profile technique assumes that the aggradation process is continuous and negligible in duration compared to the
50 post-depositional exposure, and that the inheritance is negligible or constant (Braucher et al., 2009; Laloy et al.,
51 2017). Successful applications of CRNs to date Quaternary deposits include (glacio)fluvial terraces (e.g., Rixhon
52 et al., 2011; 2014; Xu et al., 2019), alluvial fans (e.g., Rodés et al., 2011) or glacial moraines (e.g., Schaller et al.,
53 2009) that underwent negligible or constant erosion rates over the time of exposure (Braucher et al., 2009).

54 Depositional sequences can show discontinuous aggradation modes limiting the applicability of classical CRN
55 depth profiling. Examples exist of Pleistocene river deposits that consist of several sedimentary cycles (Mol et al.,
56 2000; Vandenberghe, 2001; Lauer et al., 2010; 2020; Vandermaelen et al., 2022). Between the aggradation of each
57 sequence lies a potential phase of landscape stability or erosion, hereafter referred to as a hiatus. While short
58 hiatuses in the deposition process are in principle undetectable from a depth profile, recent work by e.g.
59 Vandermaelen et al. (2022) showed that > 5000 yr long hiatuses leave a clear imprint on the CRN depth profile.
60 Further development of the classical depth profile technique is necessary to account for multiple aggradation
61 phases and modes when constraining the history of depositional landforms like braided river deposits (Nichols et
62 al., 2002; 2005; Balco et al., 2005; Dehnert et al., 2011; Rixhon et al., 2011; 2014; Rizza et al. 2019).

63 In this study, we evaluate whether it is possible to reconstruct the aggradational mode of Pleistocene braided river
64 deposits based on in situ produced CRN data collected over a ~7 m thick sedimentary sequence. We developed a

65 numerical model that simulates the accumulation of cosmogenic radionuclides, ^{10}Be and ^{26}Al , in a sedimentary
66 sequence; and that accounts for deposition and erosion phases and post-depositional exposure. The model is
67 applied to Pleistocene gravel deposits, the Zutendaal gravels. The 7 to 15 m thick gravel sheets of the Zutendaal
68 Formation are found in NE Belgium, and are assumed to be of Middle Pleistocene age (Paulissen, 1983; Gullentops
69 et al., 2001; Beerten et al., 2018). The thickness of the deposits, availability of geochemical proxy data and good
70 preservation make them an excellent candidate for this study on complex aggradation modes.

71

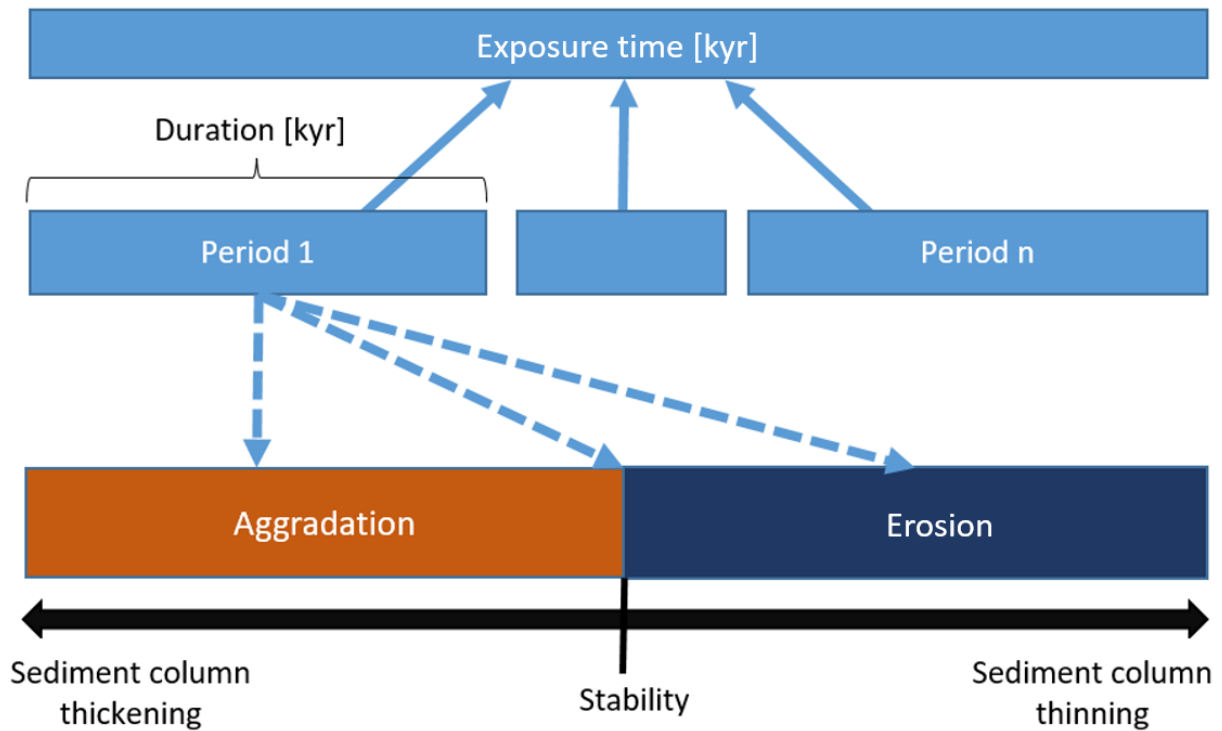
72 **2 Material and methods**

73 **2.1 Accumulation of CRN over time**

74 **2.1.1 Principles of numerical model**

75 The model simulates the buildup of (i) a sedimentary sequence including phases of aggradation, non-deposition
76 and erosion, and (ii) the **in situ** produced cosmogenic radionuclide concentrations in the sedimentary column. The
77 exposure time of the sequence corresponds to the time elapsed since the onset of the deposition (i.e., aggradation)
78 of the oldest, bottommost **layer**. The model treats the exposure time as the sum of a discrete number of time periods
79 of variable duration [kyr] (Fig. 1). During a time period, there is either deposition of sediments with a given
80 thickness [cm] on top of the pre-existing column (aggradation phase), surface erosion of a given amount of
81 sediments [cm] (erosion phase) or landscape stability (no addition nor removal of sediments). The model allows
82 to specify the lower and upper bounds of the duration of the time periods, and the amount of aggradation/erosion.

83 **A time period characterized by either stability or erosion can be defined to represent an interruption in the**
84 **aggradation process, but also the (often much longer) post-depositional time.** In the following sections, the total
85 length of all aggradation, erosional or stable phases is referred to as the “**total formation time** [kyr]”, whereas the
86 period of time after abandonment is cited as the “post-depositional time [kyr]”. **The sum of the two thus represents**
87 **the exposure time [kyr].**



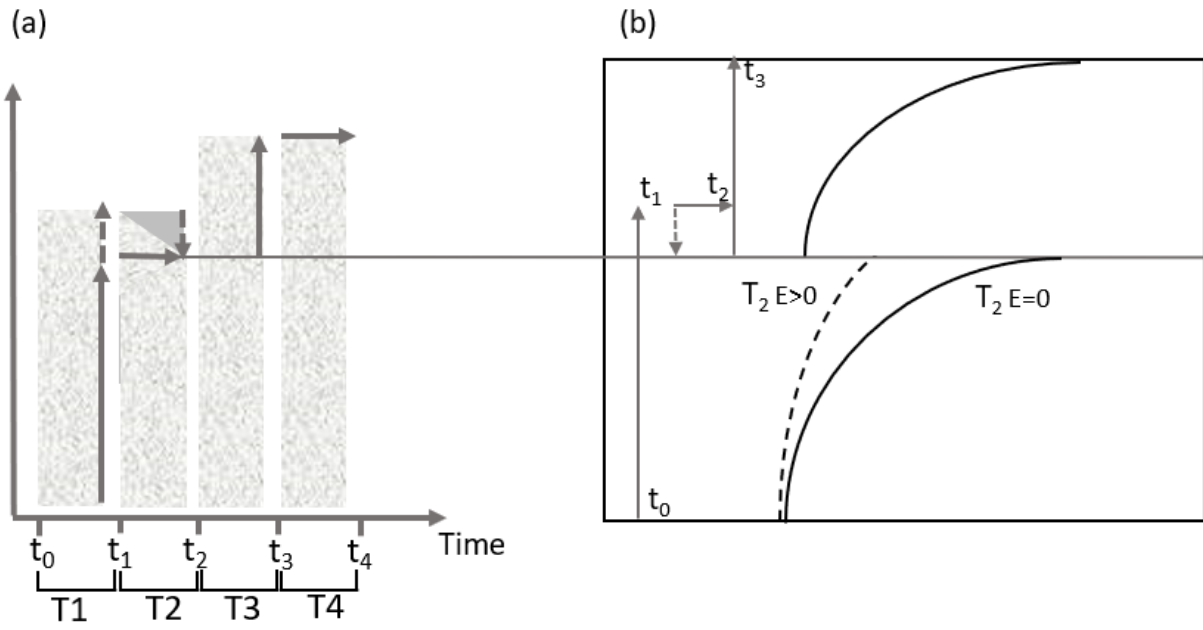
88

89 **Figure 1: Structure of the model. The total exposure time is divided in a number of time periods, during**
 90 **which the sediment column is building up (aggradation phase), eroding (erosion phase) or not changing**
 91 **(stability).**

92

93 The functioning of the model is exemplified in Fig. 2, where an example is given for the buildup of a sedimentary
 94 column in three phases. During a first time period, T1, from t_0 until t_1 , the deposition starts during an aggradation
 95 phase. **Aggradation** is then interrupted by an erosion phase of duration T2, lasting from t_1 until t_2 . After erosion, a
 96 new aggradation phase of duration T3 occurs between t_2 and t_3 . After that, the fluvial sequences are abandoned
 97 and preserved until now, i.e. the end of the exposure time. The depth variation of in situ produced cosmogenic
 98 radionuclides in the sedimentary sequence shows the effect of the complex aggradation history (Fig. 2) with two
 99 superimposed CRN depth profiles. The lower CRN depth profile developed between t_0 and t_1 , and was truncated
 100 during the erosion phase of T2. If the profile was buried at great depth (**typically > 10 m**) and shielded from cosmic
 101 rays, no further accumulation of CRN occurred after t_2 . The upper CRN depth profile developed since the onset of
 102 the T3 aggradation phase, and the buildup of CRN continued after abandonment of the sequence. Such
 103 discontinuous aggradation mode creates a CRN concentration-depth profile that cannot properly be explained by
 104 model descriptions of classical “simple” CRN depth profiles.

105



106

107 **Figure 2: Illustration of the effect of discontinuous aggradation on the depth profile of cosmogenic**
 108 **radionuclide concentrations. (a) The sedimentary sequence consists of two aggradation phases (T1 and T3)**
 109 **that are interrupted by erosion or stability during T2. (b) The in situ produced CRN profile shows two**
 110 **superimposed classical CRN depth profiles. The lower part of the profile represents two depth profiles: the**
 111 **dashed line illustrates the CRN depth profile when T2 undergoes erosion ($E > 0$), the solid line the CRN**
 112 **depth profile when T2 corresponds to a stability phase ($E=0$).**

113

114

115 2.1.2 Model equations

116 The production rate of **in situ** cosmogenic radionuclides at a given depth, z [cm], in a sedimentary deposit can be
117 described as follows:

$$118 P_i(z) = P_i(z_0) \cdot e^{\left(\frac{-z \cdot \rho}{\Lambda_i}\right)} \quad (1)$$

119 $P_i(z_0)$ [at. $\text{g}_{\text{qtz}}^{-1} \text{yr}^{-1}$] is the production rate of CRN (^{10}Be or ^{26}Al) at the surface, $z = z_0$ [cm], via the production
120 pathway i , denoting either spallation by neutrons, or capture of fast or negative muons. The attenuation length, Λ_i
121 [g cm^{-2}], is a measure of the attenuation of CRN production with depth, and was set to 160, 1500, and 4320 g cm^{-2}
122 for the production by respectively neutrons, negative muons and fast muons (Braucher et al., 2011). The dry bulk
123 density of material is written as ρ [g cm^{-3}]. The model predefines the sea level high latitude (SLHL) production
124 rate for ^{10}Be at 4.25 ± 0.18 at. $\text{g}_{\text{qtz}}^{-1} \text{yr}^{-1}$ (Martin et al., 2017), and the value is then scaled based on latitude and
125 altitude of the site following Stone (2000). The relative spallogenic and muogenic production rates are based on
126 the empirical muogenic-to-spallogenic production ratios established by Braucher et al. (2011), using a fast muon
127 relative production rate at SLHL of 0.87 % and slow muon relative production rate at SLHL of 0.27 % for ^{10}Be ,
128 and respectively 0.22 % and 2.46 % for ^{26}Al .

129 The CRN concentration changes as function of time and depth following Dunai (2010):

$$130 C(z, t) = C_{inh} \cdot e^{-\lambda \cdot t} + \sum_i \frac{P_i(z)}{\lambda + \frac{\rho \cdot \varepsilon}{\Lambda_i}} \cdot e^{-\frac{\rho \cdot (z_0 - \varepsilon \cdot t)}{\Lambda_i}} \cdot \left(1 - e^{-\left(\lambda + \frac{\rho \cdot \varepsilon}{\Lambda_i}\right) \cdot t}\right) \quad (2)$$

131 Where C_{inh} [at. $\text{g}_{\text{qtz}}^{-1}$] is the concentration of inherited CRNs from previous exposure before or during transport to
132 the final sink, λ [yr^{-1}] is the nuclide decay constant and ε is the erosion rate [cm yr^{-1}]. We used a half-life of 1387
133 kyr for ^{10}Be (Korschinek et al., 2010; Chmeleff et al., 2010) and 705 kyr for ^{26}Al (Nishiizumi, 2004).

134 The model simulates the CRN concentrations during the buildup of a sedimentary column, and considers phases
135 of aggradation, stability and erosion. The model is discretized in 1 cm depth slices. The aggradation/erosion rate
136 [cm yr^{-1}] is obtained by dividing the total thickness of the sediments deposited/eroded during one sedimentary
137 phase by the duration of the phase. Then, the model calculates the corresponding thickness [cm] of the layer to be
138 aggraded/removed per aggradation/erosion phase in function of the aggradation/erosion rate. Aggradation phases
139 are discretized in time steps of 1 kyr. The thickness of material to be aggraded is distributed equally over each
140 time step of the aggradation phase. When the value is not discrete, the model keeps track of remaining values and

141 adds it to the thickness to be aggraded over the next time step. For every cm added on top of the column, the depth
142 values are dynamically adjusted, and change from z to $z+1$. Compared to earlier work by e.g. Nichols et al. (2002)
143 or Rizza et al. (2019), the advantage of our approach is the flexible set-up of the model whereby the user can tune
144 the model complexity and its parameters easily as to adapt it to a specific study case.

145 At each time step, the concentration of ^{10}Be and ^{26}Al along the depth profile is dynamically adjusted taking into
146 account the production/removal of CRNs during each phase (erosion/stability) or time step. The inherited and the
147 in situ produced CRN concentrations are corrected for the natural decay of ^{10}Be and ^{26}Al in function of the
148 remaining exposure time. The radioactive decay of CRN becomes important for Middle to Late Pleistocene
149 deposits, and is explicitly accounted for in contrast with earlier work by e.g. Nichols et al. (2002; 2005). The ^{26}Al
150 and ^{10}Be in situ production rates and the inherited concentrations are predefined in the model. By default, the
151 model assumes that all sediments arrive in their final sink with an inherited $^{26}\text{Al}/^{10}\text{Be}$ ratio equal to the surface
152 production ratio which is set at 6.75 (Nishiizumi et al., 1989; Balco and Rovey, 2008; Margreth et al., 2016). The
153 $^{26}\text{Al}/^{10}\text{Be}$ ratio of the inherited CRNs can be adjusted in the model, to allow for simulations with a $^{26}\text{Al}/^{10}\text{Be}$
154 production ratio of 8.0 to 8.4 at depth as reported by Margreth et al. (2016) and Knudsen et al. (2019). Such
155 simulations could then represent the aggradation of material that is sourced by deep erosion by e.g. (peri)glacial
156 processes (Akcar et al., 2017, Claude et al., 2017).

157

158 2.1.3 Fitting model outputs to ^{10}Be and ^{26}Al observed data

159 We used the reduced chi-squared value as optimization criterion. The null hypothesis stipulates that the probability
160 of finding a chi-squared value higher than the one that we measure is likely. In that case, the expected distribution
161 cannot be rejected and is conserved as a possible solution. After each model simulation, the reduced chi-squared
162 value (Taylor, 1997) is derived following Eq. (3).

$$163 \quad \chi^2 = \frac{1}{d} \sum_{i=1}^n \left(\frac{(Y_i^{\text{obs}} - Y_i^{\text{mod}})}{\sigma_i} \right)^2 \quad (3)$$

164 Where $Y_i^{\text{obs}} - Y_i^{\text{mod}}$ is the difference between observed and modelled ^{26}Al and ^{10}Be concentrations, σ_i is the
165 standard error encompassing all process and analytical errors, and d corresponds to the degrees of freedom of the
166 dataset that is equal to the number of observations less the number of unconstrained model parameters. For each
167 simulation, the measured reduced chi-squared and its associated probability of finding a reduced chi-squared χ^2 of

168 higher value is reported. The null hypothesis was rejected at 0.05 significance level, and the parameters of the
169 associated simulation are stored as possible solutions.

170

171 2.2 Study area

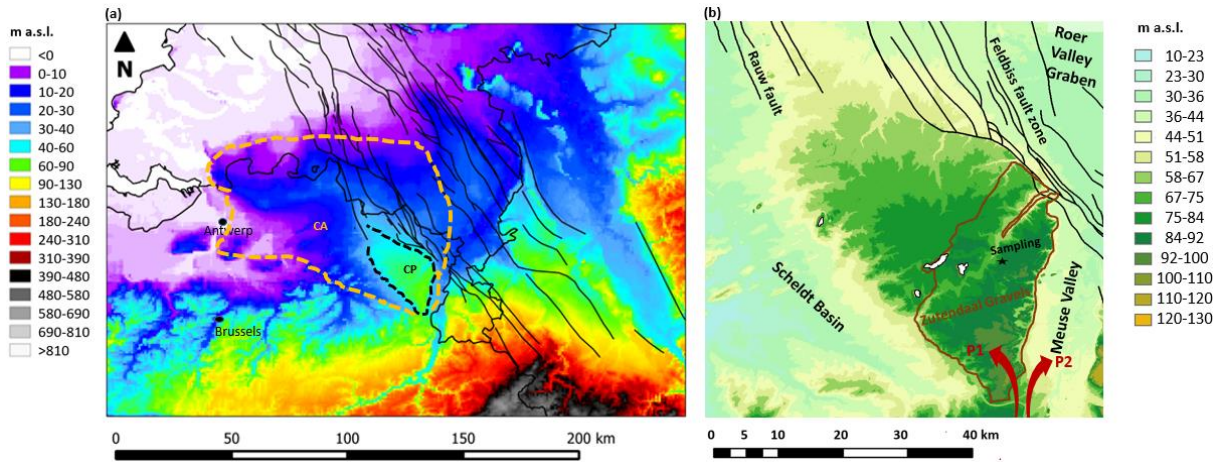
172 We selected a study site in the Zutendaal gravels, a **fluvial deposit** covering the western part of the Campine Plateau
173 (Fig. 3a). The Campine Plateau is a **relict** surface standing out of the otherwise flat Campine area, a characteristic
174 lowland of the European Sand Belt. This landscape is primarily a result of periglacial, fluvial and aeolian processes
175 related to glacial-interglacial climatic cycles that took place during the Pleistocene (Vandenberghe, 1995). It is
176 bordered in the east by the terrace staircase of the Meuse valley and in the northeast by tectonic features, the
177 Feldbiss fault zone and the Roer valley graben (Fig. 3b). In the southwest, the Campine Plateau is bordered by a
178 cryopediment shaping the transition to the Scheldt Basin (Beerten et al., 2018, and references therein).

179 The Zutendaal gravels were deposited by the **Meuse River during** the course of the Early and/or Middle Pleistocene
180 (Beerten et al., 2018, Fig. 3b). By this time, the region corresponded to a wide and shallow river valley occupied
181 by braided river channels (De Brue et al., 2015; Beerten et al., 2018 and references therein). The Zutendaal gravels
182 are structured as superposed units that possibly represent different aggradation phases related to various deposition
183 modes of braided rivers (Paulissen, 1983; Vandermaelen et al., 2022). **Architectural elements that support the**
184 **existence of individual aggradation phases include gravel bars and bedforms, channels, sediment gravity flows and**
185 **overbank fines (Dehaen, 2021). Such an assemblage approaches the structure of shallow gravel-bed braided rivers,**
186 **defined as Scott type fluvial deposits by Miall (1996), but have an unusual presence of clay plugs. After deposition**
187 **of the gravels, the Campine area was subject to erosion (Beerten et al., 2013; Laloy et al., 2017). The erosion-**
188 **resistant cap of gravel deposits played an important role in the Quaternary landscape evolution of the Campine**
189 **area: the Zutendaal gravels are now observed at the highest topographic position in the Campine landscape as**
190 **result of relief inversion (Beerten et al., 2018) whereby the gravel sheet has been covered by wind-dominated**
191 **Weichselian sands of the Opgrimbie Member, Gent Formation (Beerten et al., 2017). Optically stimulated**
192 **luminescence dating indicates an age range between ca. 23 ka and ca. 11 ka, covering the late Pleniglacial and**
193 **Late Glacial (MIS2; Derese et al., 2009; Vandenberghe et al., 2009).**

194 The age control on aggradation and post-depositional erosion is poor, but the onset of aggradation is commonly
195 assumed not to be older than 1000 ka (van den Bergh, 1996; Van Balen et al., 2000; Gullentops et al., 2001;

196 Westerhoff et al., 2008). The onset of post-depositional erosion remains unknown, but post-depositional erosion
 197 did not start before 500 ka (van den Bergh, 1996; Van Balen et al., 2000; Westerhoff et al., 2008). The specific
 198 duration and mode of aggradation of the Zutendaal gravels remain currently unresolved.

199



200

201 **Figure 3: (a) Location of the Campine Plateau (black dashed line) in the low-lying region of the Campine**
 202 **area (CA, delineated by orange dashed line) on a DTM (DTM: GTOPO30; data available from the U.S.**
 203 **Geological Survey), with indications of main faults (data available from <https://www.dov.vlaanderen.be>).**
 204 **The whole area belongs to the sandy lowlands of the European Sand Belt. The Campine Plateau stands out**
 205 **of its environment by > 50 m. (b) The Zutendaal gravels (delineated with brown line) cover the southeastern**
 206 **region and the most elevated parts of the plateau (DTM: Digitaal Hoogtemodel Vlaanderen II, DTM, raster,**
 207 **1 m; data available from overheid.vlaanderen.be). They were deposited by the Meuse River by the time it**
 208 **was flowing westward (red arrow, P1). Later on, this course was abandoned as the Meuse River moved**
 209 **eastward to form the present-day Meuse valley (red arrow, P2).**

210

211 2.3 Sampling and laboratory treatment

212 We sampled an abandoned gravel pit at the geosite “Quarry Hermans” (Bats et al., 1995) in As (51°00′29.10” N
213 5°35′46.19 E, Fig. 3), where the Zutendaal gravels are exposed over a thickness of about 7 m. At least a comparable
214 thickness of the Zutendaal gravels is supposed to be present underneath the exposure. The gravel sheet is covered
215 by 60 cm of coversands whereby the top of the profile reaches an altitude of 85 m a.s.l.. The section was described
216 in the field with annotation of grain size and sorting, sedimentary structures, and traces of chemical weathering
217 including oxidation (Vandermaelen et al., 2022). These observations allowed the subdivision of the profile in 6
218 units (U1-U6, Fig. 4). Over the depth range of 70 to 660 cm, we took 37 bulk samples for grain size and bulk
219 elemental analyses. Seventeen samples were processed for in situ produced CRN analyses: 14 for ^{10}Be to construct
220 a depth profile and 3 for ^{26}Al to analyze the $^{26}\text{Al}/^{10}\text{Be}$ ratio in the main sedimentological units of the profile. Given
221 that the uncertainties on ^{26}Al quantifications are larger than those for ^{10}Be , because of the necessity to perform
222 additional measurements of stable ^{27}Al on ICP-AES, the number of ^{10}Be samples outnumbers the ^{26}Al samples.

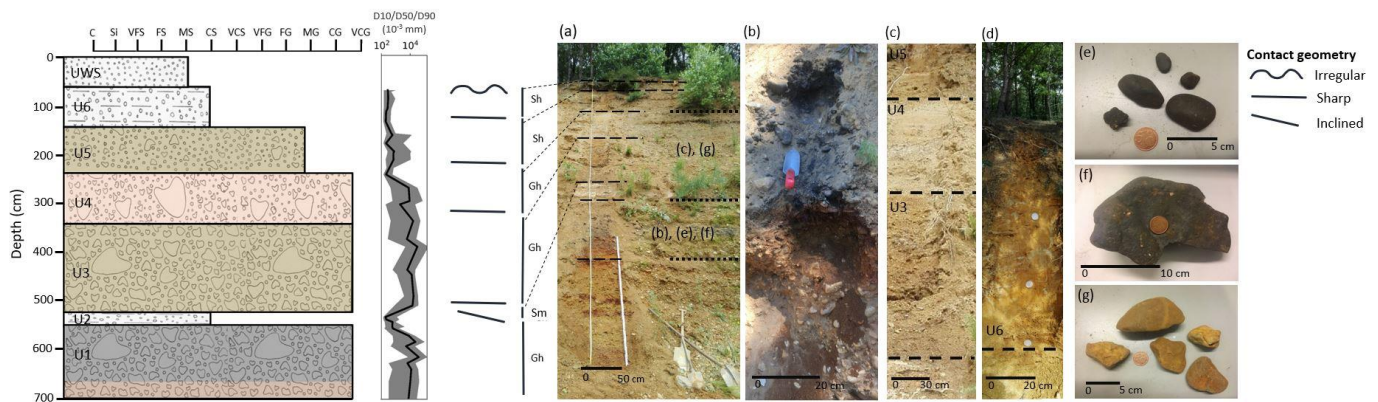
223 Samples were processed for in situ cosmogenic ^{10}Be and ^{26}Al analyses following Vanacker et al. (2007; 2015).
224 Samples were washed, dried, and sieved, and the 500–1000 μm grain size fraction was used for further analyses.
225 Chemical leaching with low concentration of acids (HCl, HNO_3 , and HF) was applied to purify quartz in an
226 overhead shaker. Later on, purified samples of 10-40 g of quartz were leached with 24 % HF for 1 h to remove
227 meteoric ^{10}Be . This was followed by spiking the sample with ^9Be and by total decomposition in concentrated HF.
228 About 0.200 mg of ^9Be was added to samples and blanks. The Beryllium in solution was then extracted by ion
229 exchange chromatography as described in von Blanckenburg et al. (1996). Three laboratory blanks were processed.

230

231

232

233



234 **Figure 4: Field observations used to constrain simulations. The log illustrates six units, labelled from U1 to**
235 **U6, that were defined based on grain size, contact geometry, sedimentary structure, sorting and weathering**
236 **traces observed in the field. They are covered by Weichselian, aeolian coversands (abbreviated UWS). U1,**
237 **U3 and U4 present imbrication and represent crudely bedded gravels (Gh). U2, U5 and U6 represent**
238 **horizontally bedded sands (Sh) or pebbly fine to very coarse sand (Sp).The granulometry is illustrated by**
239 **the D50 (black line), and the limits of the shaded area define the D10 on the left and the D90 on the right of**
240 **the black line. Panels (a) to(d) Represent illustrations of the different units. Panels (e)-(f) represent very**
241 **coarse gravels collected in U1 and showing Mn coatings. Panel (g) illustrates weathered gravels from U3**
242 **showing Fe coatings.**

243 The $^{10}\text{Be}/^9\text{Be}$ and $^{26}\text{Al}/^{27}\text{Al}$ ratios were measured using accelerator mass spectrometry on the 500 kV Tandy facility
244 at ETH Zürich (Christl et al., 2013). The $^{10}\text{Be}/^9\text{Be}$ ratios were normalized with the in-house standard S2007N and
245 corrected with the average $^{10}\text{Be}/^9\text{Be}$ ratio of three blanks of $(1.3 \pm 0.6) \times 10^{-14}$. The analytical uncertainties on the
246 $^{10}\text{Be}/^9\text{Be}$ ratios of blanks and samples were then propagated into the one standard deviation analytical uncertainty
247 for ^{10}Be concentrations. We then plotted the ^{10}Be concentrations and their respective uncertainties as function of
248 depth below the surface.

249 We measured the ^{27}Al concentrations naturally present in the purified quartz by inductively Coupled Plasma-
250 Atomic Emission Spectroscopy (Thermo Scientific iCAP 6000 Series) at the MOCA platform of UCLouvain in
251 Louvain-la-Neuve, Belgium. The $^{26}\text{Al}/^{27}\text{Al}$ results measured at ETH Zürich were calibrated with the nominal
252 $^{26}\text{Al}/^{27}\text{Al}$ ratio of the internal standard ZAL02, equal to $(46.4 \pm 0.1) \times 10^{-12}$. We subtracted from each measurement
253 a $^{26}\text{Al}/^{27}\text{Al}$ background ratio of $(7.1 \pm 1.7) \times 10^{-15}$ (Lachner et al., 2014). We reported analytical uncertainties with
254 one standard deviation, that include the propagated error of 24 % coming from the background, the uncertainty
255 associated with AMS counting statistics, the AMS external error of 0.5 % and the 5 % stable ^{27}Al measurement
256 (ICP-AES) uncertainty. The accuracy of the element chemistry was tested with reference material BHVO-2, and
257 the analytical uncertainty was evaluated at $< 3\%$ for major element concentrations and $< 6\%$ for trace element
258 concentrations (Schoonejans et al., 2016).

259

260 **2.4 Scenarios to constrain the geomorphic history of fluvial deposits**

261 We implemented 4 scenarios in our model. Each scenario consists of a succession of “n” time periods referred to
262 as T_i , that corresponds to the interval $[t_{i-1}, t_i]$, with i representing the limits of a time period in the geomorphic
263 history. Parameters are listed in Table 1. The periods are characterized by a single geomorphic setting (i.e., E =
264 erosion, A = aggradation, S = stability) whereby a given thickness of sediment is removed or aggraded [cm] over
265 a certain time interval [kyr]. Durations and thicknesses are sampled from a uniform distribution, whose upper and
266 lower bounds are stated between squared brackets in Table 1. Inheritance parameters were sampled from a normal
267 distribution (with mean and standard deviation reported in Table 1) that is centered on the inheritance that was
268 reported in previous studies on Quaternary Meuse deposits (Rixhon et al., 2011; Laloy et al., 2017). A uniform
269 bulk density of 2.1 g cm^{-3} was used, based on bulk density measurements of 17 samples. The 4 scenarios are
270 summarized in Fig. 5.

271 We ran each scenario 10^7 times with 6.75 as inherited $^{26}\text{Al}/^{10}\text{Be}$ ratio, and then again 10^7 times with a ratio of 7.40.
272 The latter is a mean value between the $^{26}\text{Al}/^{10}\text{Be}$ ratio for production at the surface and the ratio observed at depth
273 by e.g. Margreth et al. (2016). By varying the inherited $^{26}\text{Al}/^{10}\text{Be}$ ratio, we aim to account for a potential mix of
274 sediments sourced by deep and surface erosion. A plot of a kernel-density estimates using Gaussian kernels was
275 then generated from the simulations that were considered to be possible solutions based on their associated reduced
276 chi-squared value. For each parameter, the value representing the highest density of solutions is given as the
277 optimal model outcome, and the uncertainties are reported with 95% confidence intervals (2σ).

278
279
280
281
282

Table 1: Description of four scenarios that are used to constrain the geomorphic history of fluvial deposits. The different periods are presented in the headers. Each period is characterized by aggradation (A), stability (S) or erosion (E), a specific duration, a thickness to aggrade or remove and an inherent concentration. When uniform distributions are used, the lower and upper bounds of the interval are given between squared brackets. When values are depicted in a normal distribution, the mean and standard deviation are given between round brackets.

	T1 [t ₀ , t ₁]	T2 [t ₁ , t ₂]	T3 [t ₂ , t ₃]	T4 [t ₃ , t ₄]	T5 [t ₄ , t ₅]	T6 [t ₅ , t ₆]	T7 [t ₆ , t ₇]	T8 [t ₇ , t ₈]
Scenario 1								
Duration (kyr)	[500,1000]	1 or 10 (fixed)	[12,20]					
Geomorphic process	E of U6	A of UWS	E of UWS					
Thickness (cm)	[0,500]	[60,200]	(A of UWS)-200					
Inheritance (x 10 ³ at.g _{qtz} ⁻¹)	Normal(90; 20)	/	/					
Scenario 2								
Duration (kyr)	[500,1000]	[1,10]	1 or 10 (fixed)	[12,20]				
Geomorphic process	S	E of U6	A of UWS	E of UWS				
Thickness (cm)	0	(A of U4/5/6) -275	[60,200]	(A of UWS)-200				
Inheritance (x 10 ³ at.g _{qtz} ⁻¹)	Normal(90; 20)	/	/	/				
Scenario 3								
Duration (kyr)	[0,60]	1 or 10 (fixed)	[0,60]	1 or 10	[500,1000]	1 or 10 (fixed)	[12,20]	
Geomorphic process	E of U1/U2	A of U3	E of U3	A of U4/U5/U6	E of U6	A of UWS	E of UWS	
Thickness (cm)	[0,500]	[185,685]	(A of U3)-185	[275,775]	0	[60,200]	(A of UWS)-200	
Inheritance (x 10 ³ at.g _{qtz} ⁻¹)	Normal(90; 20)	Same as U1/U2	/	Same as U1-U2	/	/	/	
Scenario 4								
Duration (kyr)	[0,60]	1 or 10 (fixed)	[0,60]	1 or 10	[500,1000]	[1,10]	1 or 10 (fixed)	[12,20]
Geomorphic process	E of U1/U2	A of U3	E of U3	A of U4/U5/U6	S	E of U6	A of UWS	E of UWS
Thickness (cm)	[0,500]	[185,685]	(A of U3)-185	[275,775]	0	(A of U4/5/6) -275	[60,200]	(A of UWS)-200
Inheritance (x 10 ³ at.g _{qtz} ⁻¹)	Normal(90; 20)	Same as U1/U2	/	Same as U1-U2	/	/	/	/

283

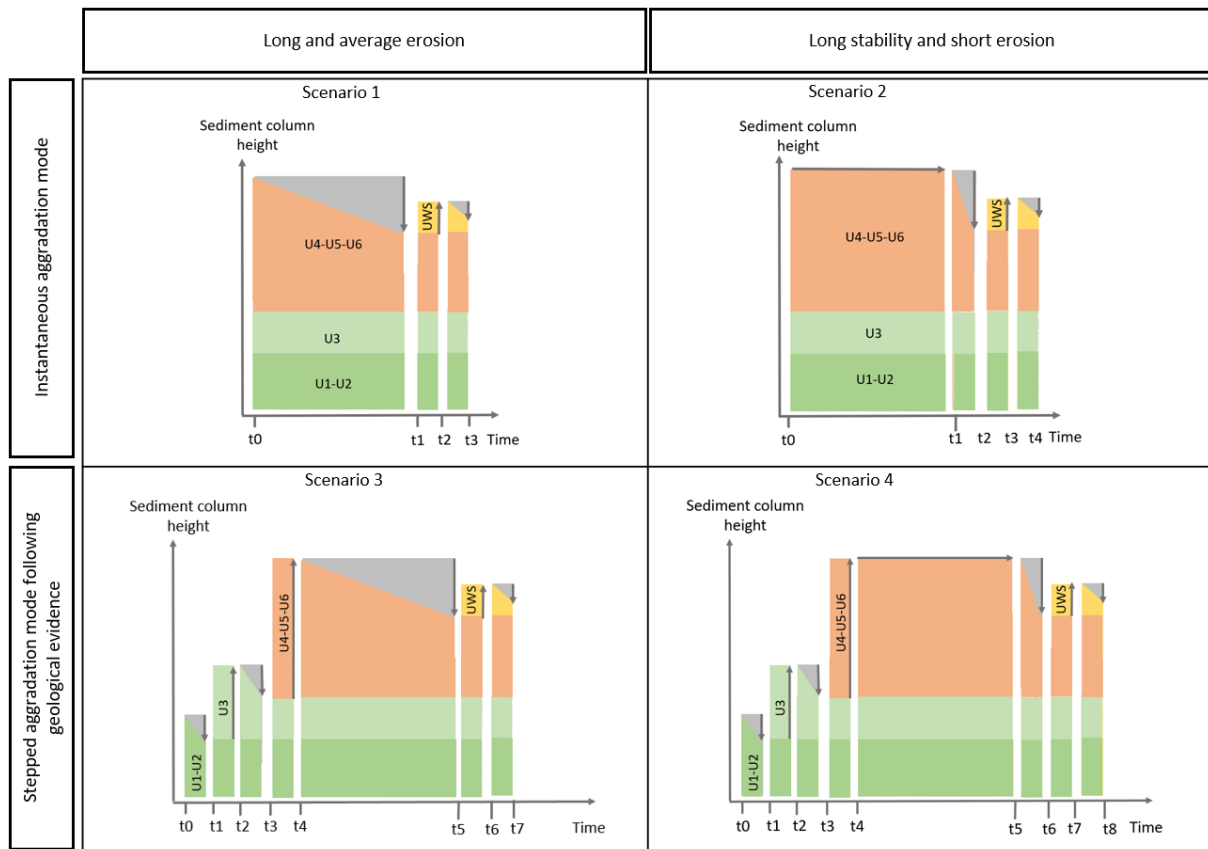
284 Based on prior information on the evolution of the Zutendaal gravels, four constraints were defined:

- 285 1) “Not longer than”: The total geomorphic history takes place over the last 1000 kyr (Beerten et al.,
286 2018, and references therein). In consequence, any scenario for which the total duration exceeded
287 1000 kyr was automatically discarded.
- 288 2) “Not shorter than”: In the area where the Zutendaal gravels are currently outcropping, deposition
289 ended by 500 ka at the latest (Westerhoff et al., 2008). The abandonment of the terrace must be older
290 than 500 ka.
- 291 3) “Final thickness of every unit should correspond to the measured thickness”. After an aggradation
292 phase, the thickness of the unit can decrease by erosion over the following time period until it matches
293 the observed, present-day thickness.
- 294 4) The two last time periods of any scenario should include 60 to 200 cm aggradation of Weichselian
295 coversands (Unit Weichselian coversands, abbreviated “UWS”), followed by an erosion phase until
296 the thickness of the coversands matches the present-day thickness.

297 The model was run for each scenario using the constraints and parameter distributions of Table 1. Parameter values
298 were attributed randomly following Hidy et al. (2010). The two first scenarios, scenarios 1 and 2, represent the
299 classical depth profile (Braucher et al., 2009): scenario 1 represents a long and constant post-depositional erosion
300 phase whereas scenario 2 represents a long stable phase that is followed by a recent, pre-Weichselian, episode of
301 rapid erosion. In scenario 1, the fluvial gravel sheet starts accumulating CRN over a [500, 1000] kyr period that is
302 characterized by constant erosion of [0, 500] cm. In contrast, in scenario 2, the fluvial sheet remains stable over
303 T1 and then undergoes a rapid erosional phase of [0, 500] cm over 1 or 10 kyr (T2). The maximum erosion rate is
304 thus 500 cm in 1 kyr, or 5 mm yr⁻¹, and is based on the upper range of long-term erosion rates reported in literature
305 (Portenga and Bierman, 2011; Covault et al., 2013). After erosion, the fluvial sheet is covered by Weichselian
306 coversands (UWS) during a 1 to 10 kyr period. The sand deposit is then eroded until it reaches the present-day

307 thickness of 60 cm. In both scenarios, the onset of the in situ CRN accumulation is concomitant with the beginning
 308 of the post-depositional period (Fig. 5).

309



310

311 **Figure 5: The four scenarios that are developed to represent the sedimentary sequence of the Zutendaal**
 312 **gravels in As. Grey arrows represent aggradation (upward arrow), erosion (downward arrow) or stability**
 313 **(horizontal arrow). The material that is removed by erosion is coloured in grey.**

314 In contrast to the instantaneous aggradation mode of scenarios 1 and 2, the scenarios 3 and 4 consider a stepped
 315 aggradation mode and are based on ancillary data from geochemical proxies (Vandermaelen et al., 2022). As
 316 illustrated in Fig. 5, the simulations start with unit U1-U2 in place at the bottom of the sedimentary sequence. This
 317 is followed by different phases of aggradation and erosion. The duration of any erosion phase is set to a maximum
 318 of 60 kyr, so that two erosion phases account for a maximum of 120 kyr. This corresponds to the duration of a full
 319 glacial cycle, i.e. about 110 to 120 kyr, based on Busschers et al. (2007). The first phase of erosion of [0, 500] cm
 320 is thus simulated over a T1 period of [0, 60] kyr. This is followed by the T2 period with [185, 685] cm aggradation
 321 of unit U3. The minimum aggradation corresponds to the present-day thickness of U3, and takes place during a

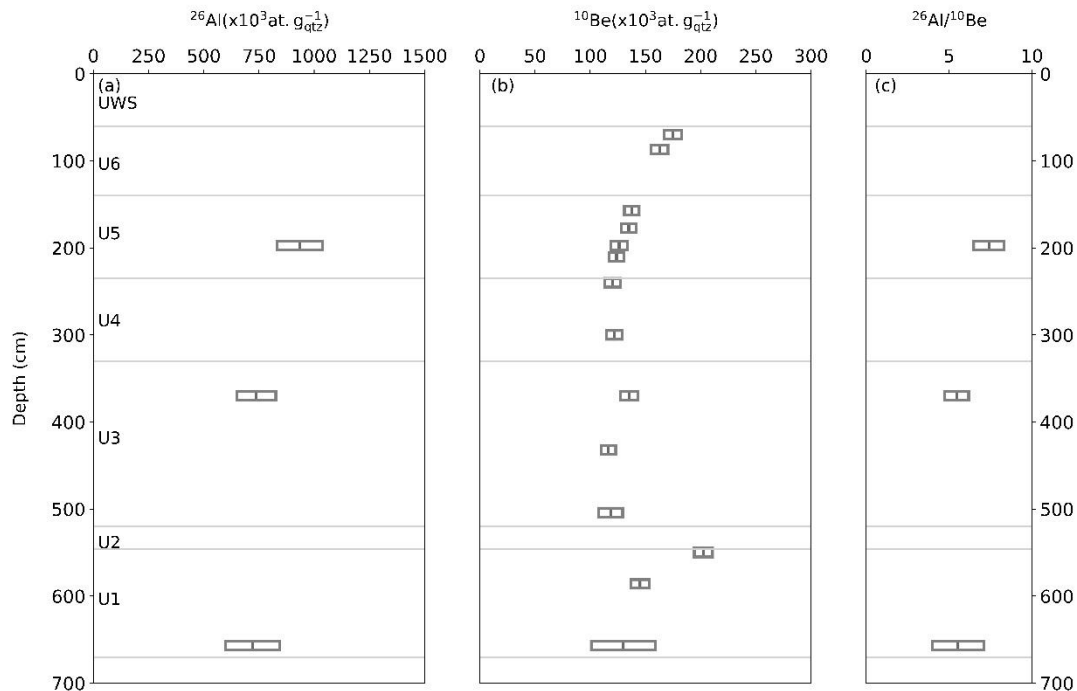
322 single step, 1 kyr, or 10 kyr (Table 1). During the T3 period, the thickness of U3 that exceeds 185 cm is eroded
323 over [0, 60] kyr. The next aggradation phase, T4, is characterized by [275, 775] cm aggradation of units U4, U5
324 and U6 over 1 or 10 kyr. The minimum aggradation corresponds to their present-day thickness. After this phase,
325 the post-depositional evolution of the fluvial sequence starts: in scenario 3, the thickness of U4, U5 and U6 that
326 exceeds 275 cm is then slowly and constantly eroded over [500, 1000] kyr, corresponding to the T5 period. In
327 scenario 4, there is a long phase of stability during the T5 period that is then followed by a phase of rapid erosion,
328 during the T6 period lasting [1, 10] kyr. In both scenarios, 3 and 4, the last two periods are similar to the aggradation
329 and erosion of the Weichselian coversands specified in scenarios 1 and 2.

330

331 **3 Results**

332 **3.1 In situ produced CRN concentrations along the depth profile**

333 The ^{10}Be concentrations vary from 120×10^3 to more than 200×10^3 at. $\text{g}_{\text{qtz}}^{-1}$ (Table 2). The total uncertainties on
334 the measured ^{10}Be concentrations are below 7%, with exception of the lowermost sample (Heras-02). The observed
335 CRN depth variation deviates from a simple exponential decrease of ^{10}Be concentration with depth, and points to
336 a complex deposition history. The upper 8 values (70 to 300 cm, corresponding to U6, U5 and U4) show an
337 exponential decrease from $(175 \pm 8) \times 10^3$ to $(122 \pm 7) \times 10^3$ at. $\text{g}_{\text{qtz}}^{-1}$ (Fig. 6). There is an abrupt change in the
338 concentration at 370 cm depth, corresponding to $(135 \pm 7) \times 10^3$ at. $\text{g}_{\text{qtz}}^{-1}$ measured at the top of the U3 unit, about
339 12 % higher than the sample taken at 300 cm depth. The following two samples in U3 show a steady decrease in
340 ^{10}Be concentration with depth. At the bottom of the profile, in the upper part of U1, a third local maximum of ^{10}Be
341 concentration is found. The value of $(202 \pm 8) \times 10^3$ at. $\text{g}_{\text{qtz}}^{-1}$ measured at 550 cm depth is the highest value that
342 was measured in the profile and is 50 % higher than the average ^{10}Be concentration measured in the overlying
343 units. The samples taken in U1 show a steady decrease of ^{10}Be concentration with depth, from $(145 \pm 8) \times 10^3$ at.
344 $\text{g}_{\text{qtz}}^{-1}$ at 586 cm to $(130 \pm 30) \times 10^3$ at. $\text{g}_{\text{qtz}}^{-1}$ at 657 cm depth.



345

346 **Figure 6: (a) and (b) plots present the ^{26}Al and ^{10}Be concentration, and (c) the $^{26}\text{Al}/^{10}\text{Be}$ ratio. The reported**
 347 **uncertainties are one standard deviation (1σ).**

348

349 **The three samples analyzed for ^{26}Al show a decrease of ^{26}Al concentration with depth: from $(934 \pm 103) \times 10^3$ at.**
 350 **$\text{g}_{\text{qtz}}^{-1}$ at 197 cm depth (U5) to $(734 \pm 88) \times 10^3$ at. $\text{g}_{\text{qtz}}^{-1}$ at 370 cm depth (U3) and finally to $(720 \pm 122) \times 10^3$ at.**
 351 **$\text{g}_{\text{qtz}}^{-1}$ at 657 cm depth (U1). Considering the total uncertainties of 11 to 17 % on the AMS and ICP-AES**
 352 **measurements, only the ^{26}Al concentration of the uppermost sample is significantly higher than the two deeper**
 353 **ones (Fig. 6). Although based on a limited number of samples, the depth evolution of the ^{26}Al concentrations**
 354 **differs from what is observed for the ^{10}Be concentrations as the ^{10}Be concentration appears higher at 370 cm depth**
 355 **than at 197 cm depth.**

356 **The three $^{26}\text{Al}/^{10}\text{Be}$ ratios decrease with depth with values of 7.41 ± 0.92 at 197 cm, 5.45 ± 0.73 at 370 cm and**
 357 **5.54 ± 1.55 at 657 cm). The measured ratios are consistent with near surface production (i.e., $^{26}\text{Al}/^{10}\text{Be}$ ratio of**
 358 **6.75 , Granger and Muzikar, 2001; Erlanger et al., 2012).**

359 **Table 2: In situ produced CRN concentrations. All reported uncertainties are one standard deviation (1 σ).**

Sample ¹⁰ Be	Field code	Depth (cm)	Qtz (¹⁰ Be) (g)	⁹ Be (mg)	¹⁰ Be/ ⁹ Be (x 10 ⁻¹²)	¹⁰ Be (x 10 ³ at. g _{qtz} ⁻¹)	Sample ²⁶ Al	Qtz (²⁶ Al) (g)	²⁶ Al/ ²⁷ Al (x 10 ⁻¹³)	²⁷ Al (ppm)	²⁶ Al (x 10 ³ at. g _{qtz} ⁻¹)	²⁶ Al/ ¹⁰ Be
TB3824	Heras-18	70	38.1	0.266	0.387 ± 0.015	175 ± 8						
TB3823	Heras-17	87	38.7	0.220	0.443 ± 0.018	163 ± 8						
TB3820	Heras-14	157	38.1	0.264	0.309 ± 0.012	138 ± 7						
TB3819	Heras-13	177	37.1	0.220	0.355 ± 0.014	135 ± 7						
TB3818	Heras-12	197	37.8	0.266	0.280 ± 0.014	126 ± 7	ZA2125	12.5	1.79 ± 0.20	243	935 ± 103	7.41
TB3821	Heras-15	210	38.2	0.266	0.278 ± 0.012	124 ± 7						
TB3817	Heras-11	240	38.0	0.266	0.270 ± 0.013	120 ± 7						
TB3816	Heras-10	300	37.9	0.220	0.327 ± 0.016	122 ± 7						
TB3815	Heras-09	370	37.4	0.267	0.295 ± 0.015	135 ± 8	ZA2124	10.3	1.21 ± 0.15	289	738 ± 88	5.45
TB3814	Heras-08	432	37.8	0.268	0.258 ± 0.012	116 ± 7						
TB3813	Heras-07	504	21.2	0.268	0.152 ± 0.011	118 ± 11						
TB3812	Heras-06	550	37.4	0.268	0.435 ± 0.015	202 ± 8						
TB3811	Heras-04	586	33.6	0.268	0.284 ± 0.014	145 ± 8						
TB4346	Heras-02	657	10.3	0.296	0.078 ± 0.014	130 ± 30	ZA2121	10.3	1.16 ± 0.20	296	720 ± 122	5.54
TB3829	n/a	n/a	0	0.220	0.006 ± 0.002							
TB3830	n/a	n/a	0	0.267	0.018 ± 0.005		n/a	n/a				
TB4349	n/a	n/a	0	0.219	0.015 ± 0.004							

360

361

362 **3.2 Optimal model fits**

363 The optimal model fits for the scenarios representing the instantaneous aggradation mode (i.e. scenario 1 and 2,
 364 Fig. 5) return a minimized reduced chi-squared value above 11, and fail to represent the observed ^{10}Be and ^{26}Al
 365 data correctly. Best fits for these scenarios are also insensitive to the inherited $^{26}\text{Al}/^{10}\text{Be}$ ratio. The optimal model
 366 fits for the scenario that consider a stepped aggradational mode, long and average erosion (i.e. scenario 3, Fig. 5)
 367 have a reduced chi squared value of 130 when using aggradation phases of 1 kyr, and 147 using phases of 10 kyr.
 368 The goodness-of-fit does not improve when using an inherited $^{26}\text{Al}/^{10}\text{Be}$ ratio of 7.40 instead of 6.75 (Table 3).

369 **Table 3: Reduced chi-squared values of the optimal model fits for scenario 1, 2, 3 and 4, with $^{26}\text{Al}/^{10}\text{Be}$ ratios**
 370 **of 6.75 and 7.40 and with 1 and 10 kyr durations of the aggradation phases. The star indicates whether the**
 371 **p-value did not show a significant disagreement between observed and modelled CRN concentrations.**

Inherited $^{26}\text{Al}/^{10}\text{Be}$ ratio	6.75		7.40	
Aggradation phases (kyr)	1	10	1	10
Scenario 1	123	/	123	/
Scenario 2	11.5	/	11.5	/
Scenario 3	137	147	130	155
Scenario 4	1.55*	1.44*	1.36*	1.25*

372

373 The scenarios that consider a stepped depositional history and a period of [500; 1000] kyr of landscape stability
 374 (scenarios 4) show better optimal fits (Table 3). At the 0.05 significance level, the simulations can be accepted as
 375 possible solutions when the reduced chi-squared value is below 1.83. With the inherited $^{26}\text{Al}/^{10}\text{Be}$ ratio of 6.75,
 376 the optimal simulations with aggradation phases of 1 and 10 kyr have a reduced chi-squared value of respectively
 377 1.55 and 1.44. The model fit improves when using inherited $^{26}\text{Al}/^{10}\text{Be}$ ratios of 7.40, with optimal reduced chi-
 378 squared values of respectively 1.36 and 1.25. Given that the goodness-of-fit is similar for the simulations with
 379 aggradation phases of 1 or 10 kyr, we pooled all results in the kernel-density plots. Figure 6 resumes the results on
 380 the overall aggradation time of the entire sequence, the deposition age of the lowermost unit, U1, and the duration
 381 of hiatuses and corresponding surface erosion at the top of the U2, U3 and U6 layers. **The optimal values are**
 382 **reported with their 95% confidence intervals (2σ).**

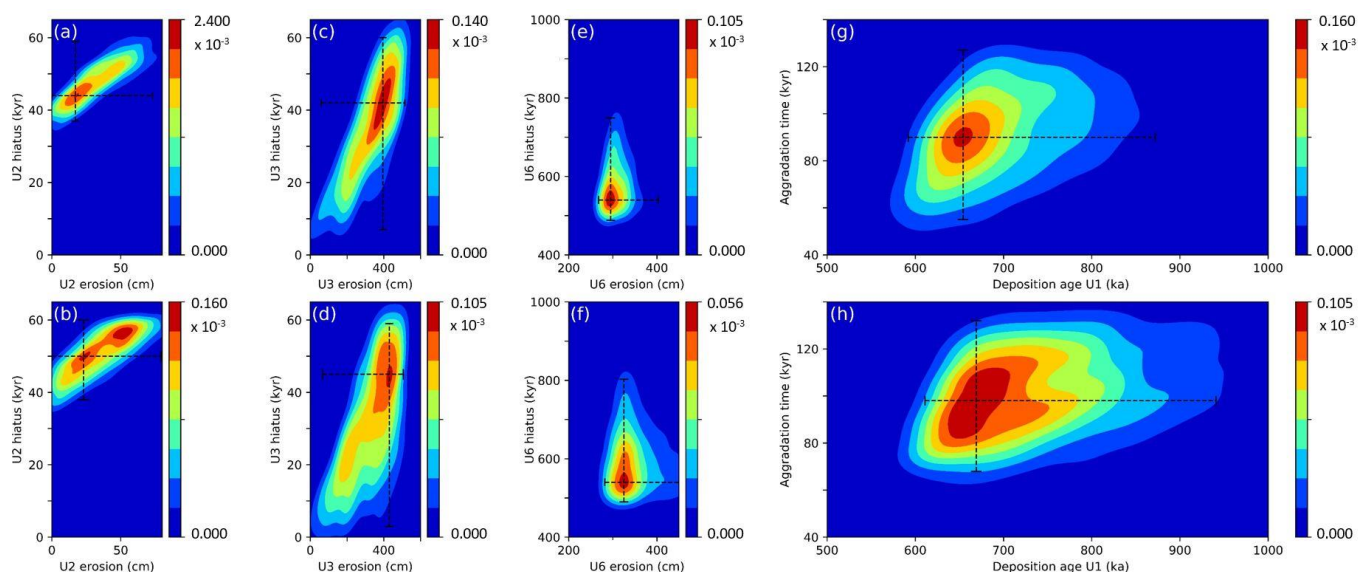
383 The hiatus at the top of the U2 unit is characterized by a duration of 44_{-7}^{+15} kyr and an erosion amount of 17_{-17}^{+56}
 384 cm in the simulations with inherited ratios of 6.75 (Fig. 7a), and 50_{-12}^{+10} kyr and 23_{-23}^{+56} cm in simulations with

385 inherited ratios of 7.40 (Fig. 7b). The combination of hiatus duration and erosion amount results in an erosion rate
386 of 4.60 m Myr⁻¹ and 3.86 m Myr⁻¹ for simulations with inherited ratios of resp. 6.75 and 7.40. Although this erosion
387 rate is one order of magnitude lower than the **median** global denudation rate (i.e., 54 m Myr⁻¹) that was calculated
388 from a set of 87 drainage basins (Portenga and Bierman, 2011), it is coherent with the lowest long-term incision
389 rate reported for the Meuse catchment near Liège (Van Balen et al., 2000).

390 For the hiatus at the top of U3, the highest density of solutions is observed around 42⁺¹⁸₋₃₅ kyr and 45⁺¹⁴₋₄₂ kyr for
391 simulations with inherited ratio of resp. 6.75 and 7.40 (Fig. 7c & d), which is similar as the hiatus' duration
392 established for the lower U2 unit. In contrast, the associated solutions for erosion are one order of magnitude higher
393 than at the top of U1-U2, with values of 395⁺¹²⁰₋₃₃₅ cm (**94 m Myr⁻¹**) and 430⁺⁷⁶₋₃₆₃ cm (**96 m Myr⁻¹**) for inherited
394 ratios of respectively 6.75 and 7.40. The hiatus on top of U6 encloses the time between the last aggradation of
395 fluvial deposits and the Weichselian coversands. The highest density of possible solutions is found at 540⁺²⁰⁹₋₅₂ kyr
396 for simulations with an inherited ratio of 6.75, and a similar value, i.e. 540⁺²⁶³₋₅₀ kyr, is found with a ratio of 7.40
397 (Fig. 7e). **The erosion of the overburden that was present on top of U6 took place before the aggradation of**
398 **Weichselian coversands, and is estimated at 295⁺²⁰⁸₋₂₇ and 325⁺¹⁵¹₋₄₃ cm for inherited ratios of resp. 6.75 and 7.40**
399 **(Fig. 7f). Constant erosion of the overburden over the period of [500; 1000] kyr is not likely (i.e. scenario 3, Table**
400 **3), and a scenario with rapid erosion of the overburden results in significantly better model fit (i.e. scenario 4,**
401 **Table 3). The current model setup fixed the time interval at [1, 10] kyr which results in optimal values of 295 and**
402 **325 m Myr⁻¹. Further research is needed to better constrain the timing and length of such an erosion phase, as they**
403 **have a strong impact on the erosion estimates.**

404 **Based on the CRN age-depth modelling, the deposition age of the bottommost deposits of the exposure was**
405 **constrained at 654⁺²¹⁸₋₆₂ and 669⁺²⁷²₋₅₈ ka for inherited ratios of resp. 6.75 and 7.40 (Fig. 7g & h). The total formation**
406 **time of the sedimentary sequence, including the aggradation phases and the sedimentary hiatuses, is estimated at**

407 90_{-45}^{+37} and 98_{-30}^{+34} kyr for inherited ratios of resp. 6.75 and 7.40 (Fig. 7g & h). The top of the Zutendaal Formation
 408 that is exposed in As has a deposition age of 562_{-45}^{+211} and 565_{-44}^{+269} ka for inherited ratios of resp. 6.75 and 7.40.



409
 410 **Figure 7: Density plot of the possible model outcomes for scenario 4. Any simulation that returned a reduced**
 411 **chi-squared smaller than 1.83 is considered to be significant, and included as a possible solution in the**
 412 **density plots. The density of significant solutions is shown by color coding. The four upper panels (a, c, e, g)**
 413 **represent the parameters of simulations (n=486) characterized by a $^{26}\text{Al}/^{10}\text{Be}$ of 6.75, and the lower panels**
 414 **(b, d, f, h) the parameters of simulations (n= 1695) with a $^{26}\text{Al}/^{10}\text{Be}$ of 7.40. For each parameter, the most**
 415 **likely value (i.e. value with highest density of significant solutions) is reported as well as its 95% confidence**
 416 **interval (2σ). The 95% confidence interval is derived from the 2.5 % and 97.5 % limits of the kernel**
 417 **cumulative density function.**

418
 419

420 4. Discussion

421 4.1 Aggradation mode of the Zutendaal gravels

422 The onset of aggradation of the Middle Pleistocene gravel deposits of the so-called Main Terrace of the Meuse in
423 NE Belgium, the Zutendaal gravels, was commonly assumed to be situated between 500 and 1000 ka (van den
424 Berg, 1996; Van Balen et al., 2000; Gullentops et al., 2001; Westerhoff et al., 2008). Here, by applying a numerical
425 model to the CRN concentration-depth profiles, the age for the onset of U1 aggradation is estimated to be 654^{+218}_{-62}
426 ka. This age, within error limits, agrees with previous correlations of the gravel sheet with the Cromerian Glacial
427 B, and marine isotope stage (MIS) 16 (Gullentops et al., 2001). Around this time, the gravel sheet was already in
428 the process of being build and only the upper part of the Zutendaal gravels (potentially 15 to 20 m thick gravel
429 sheet) is here exposed. Therefore, it cannot be excluded that the base of the (buried part of the) Zutendaal gravels
430 corresponds with MIS 18.

431 The model simulations also confirmed the existence of a stepped aggradation mode whereby phases of aggradation
432 are alternating with phases of stability or erosion. At least three phases of aggradation with two intraformational
433 hiatuses are identified: a first hiatus at the top of the U2 unit lasting 44^{+15}_{-7} kyr, and resulting in surface erosion of
434 17^{+56}_{-17} cm; a second hiatus at the top of the U3 unit of similar duration, i.e. 42^{+18}_{-35} kyr, but much higher surface
435 erosion of 395^{+120}_{-335} cm. The third and final aggradation phase (U4-U5-U6, ending at last at 562^{+211}_{-45} ka) occurred
436 before abandonment of the region by the Meuse River. The results are here reported for inherited ratios of 6.75,
437 and aggradation phases of 1 and 10 kyr, but they do not differ significantly when using alternative inherited
438 $^{26}\text{Al}/^{10}\text{Be}$ ratios (Table 3).

439 The total formation time of the sedimentary sequence exposed in As is estimated at 90^{+37}_{-45} kyr. Given that only the
440 upper 7 m are exposed in As (Gullentops et al., 2001), the deposition of the entire sequence of the Zutendaal
441 gravels probably represents more than one climatic cycle. Slow aggradation leading to ^{10}Be enrichment with depth
442 (e.g., Nichols et al., 2002; Rixhon et al., 2014) is not directly observed in this sequence. However, it could
443 eventually have occurred in the shallow and sandy unit, U2, that was not sampled for ^{10}Be . Slow aggradation
444 would further increase the total formation time. Such a prolonged formation time can occur in fluvial depositional
445 systems in the absence of tectonic uplift and consecutive river downcutting (Sougnéz and Vanacker, 2011). Only
446 after the Meuse River abandoned its northwestern course (Fig. 1), it developed a staircase of alluvial terraces in
447 response to tectonic uplift of the Ardennes-Rhenish Massif (Beerten et al., 2018 and references therein).

448 According to simulations of scenario 4, an overburden remained in place from the abandonment time until it was
449 removed by an erosion phase, which preceded the sedimentation of the Weichselian aeolian cover. Other scenarios
450 could be tested whereby the post-depositional history is characterised by alternating phases of aeolian sand
451 deposition and subsequent removal of this loose material (Beerten et al., 2017). The aeolian sand deposits that
452 cover the top of various Meuse River terraces in the northern part of the Meuse Valley are commonly assumed to
453 be Weichselian in age (e.g., Vanneste et al., 2001; Derese et al., 2009; Vandenberghe et al., 2009) regardless of
454 their morphological position and age (Paulissen, 1973). This being said, a few very thin late Saalian aeolian sand
455 deposits were found on top of the Saalian Eisden-Lanklaar terrace near the steep valley wall of the Meuse River
456 east of the study site (Paulissen, 1973). This would imply that only the latest episode of sand movement is well
457 preserved on the top of the terrace landscape, and that previous aeolian sand covers have been reworked during
458 subsequent glacial-interglacial cycles that followed the deposition of the terrace deposits.

459

460 **4.2 Added value of modeling complex aggradation modes**

461 Studies using the classical CRN depth profile approach mainly envision to deliver an exposure age of the surface,
462 i.e., of the uppermost deposits only. By using numerical modeling, it becomes possible to reconstruct the
463 aggradation time and mode of a sedimentary sequence based on the evolution of the CRN concentrations with
464 depth. This case study in NE Belgium demonstrates that the total formation time of braided river deposits, such as
465 the Zutendaal gravels, may constitute nearly 20 % of the deposition age (Fig. 7g & h). This shows the importance
466 of considering the aggradation mode of braided rivers when applying CRN techniques to > 3 m deep sedimentary
467 sequences.

468 Firstly, this approach can account for the presence of hiatuses in the sedimentary sequence. Hiatuses in the
469 aggradation process temporarily expose parts of fluvial sheets that would otherwise be buried at depth and partially
470 shielded from CRN accumulation. This can create a positive offset in the CRN concentration-depth profile,
471 whereby the concentration at a given depth is higher than the true inheritance value (Fig. 6; Vandermaelen et al.,
472 2022). Such observations do not fit in the simple concentration-depth distribution, and are often classified as
473 outliers or as results of differential inheritance (e.g., following the concepts reported by Le Dortz et al., 2012).

474 Secondly, by considering the aggradation mode, additional information on the sourcing of sediments can be
475 extracted from the depth distribution of $^{26}\text{Al}/^{10}\text{Be}$ ratios. The $^{26}\text{Al}/^{10}\text{Be}$ ratios that are measured in fluvial sediments

476 result from (i) the inherited $^{26}\text{Al}/^{10}\text{Be}$ ratios of the source material and (ii) the in situ CRN accumulation when the
477 material is exposed to cosmic rays. Accounting for the changing depth of the sedimentary layers within the fluvial
478 sheet may allow one to explain high $^{26}\text{Al}/^{10}\text{Be}$ ratios (i.e., > 6.75) measured at depth. For the case-study in NE
479 Belgium, the model fit improved slightly when an inherited $^{26}\text{Al}/^{10}\text{Be}$ ratio of 7.40 was used in the simulations
480 (Fig. 7). Inherited $^{26}\text{Al}/^{10}\text{Be}$ ratios that are substantially higher than 6.75 often point to intense physical erosion in
481 the headwater basins where material is sourced from deep erosion by e.g. (peri)glacial processes (Claude et al.,
482 2017; Knudsen et al., 2019). The material that was buried several meters below the surface is then delivered to the
483 fluvial system, and breaks in smaller parts on its route to the final sink or during intermediate storage. Such deposits
484 are then constituted of a mix of sediments characterized by different $^{26}\text{Al}/^{10}\text{Be}$ inherited ratios. In their final sink,
485 the sediments will further accumulate CRN following the $^{26}\text{Al}/^{10}\text{Be}$ surface production ratio of ~ 6.75 when exposed
486 at (or close to) the surface, or they can maintain an $^{26}\text{Al}/^{10}\text{Be}$ isotope ratio above 6.75 when quickly buried to a
487 depth above 300 g cm^{-2} where the relative production of ^{26}Al to ^{10}Be is larger due to muogenic production.

488

489 **4.3 Trade-off between model complexity and sample collection**

490 Optimization methods like the reduced chi-squared require that the number of observed data is larger than the
491 number of free parameters (Hidy et al., 2010). There is thus a trade-off to make between the complexity of the
492 model and the number of datapoints obtained by CRN analyses. In case of CRN concentration depth profiles, the
493 number of samples is often limited by the capacity and financial constraints that are needed to process samples for
494 CRN analyses. In the numerical model, the phases of aggradation are characterized by their duration, aggradation
495 thickness and inherited ^{10}Be concentration. They are followed by phases of stability or erosion with an unknown
496 duration.

497 The inclusion of aggradation modes in CRN concentration depth profile modelling therefore requires more
498 unconstrained parameters than the classical depth profile approach (Table 1). The minimum number of CRN
499 measures that is required can be calculated as follows:

$$500 \quad N_{CRN} > (k \times N_{aggrad}) + (l \times N_{erosion}) \quad (4)$$

501 Where N_{CRN} is the number of CRN measurements for individual samples, k and l are the number of unconstrained
502 parameters for respectively each aggradation and erosion/stability phase. Further complexification of the model,
503 by e.g. including unconstrained parameters for sediment density or $^{26}\text{Al}/^{10}\text{Be}$ inherited ratio, will further increase

504 the required number of CRN observations. With a limited number of samples, the complexity of the model can be
505 reduced by e.g. keeping the CRN inheritance fixed. This is acceptable when the local minima of the CRN
506 concentrations in a given sedimentary sequence are within 10 % of the mean of the lowest values. For braided
507 river deposits, it is also viable to fix the length of the aggradation phase to 1 or 10 kyr: most sedimentary sequences
508 represent long periods of non-deposition or erosion interrupted by rapid and short-lived depositional events
509 (Bristow and Best, 1993).

510

511 **4.4 Chronostratigraphical implications**

512 Based on the age of 654^{+218}_{-62} ka obtained for the base of the sedimentary sequence in As, the Zutendaal gravels
513 exposed at the geosite in As were most likely deposited during MIS 16, and the lower part maybe even during MIS
514 18 according to Northwest European chronostratigraphical subdivision and correlation with the marine isotope
515 record, Cohen and Gibbard (2011). The uppermost part of the deposits (U6, Fig. 6) in As is dated at 562^{+211}_{-45} ka,
516 thereby yielding a youngest possible deposition age of 517 ka. This age would associate the uppermost deposits
517 with MIS 14. However, it cannot be ruled out that by that time the Meuse had already shifted its course towards
518 the east of the As sampling site (Van Balen et al., 2000). If this is true, the uppermost depositional sequence in As
519 should correspond to material deposited by another local river, rather than by the Meuse itself. It is possible that
520 the Bosbeek occupied this part of the Campine Plateau after the Meuse had shifted to the east. A fossil valley floor
521 of the Bosbeek River has been identified by Gullentops et al. (1993) only a few 100 meters away from the As
522 sampling site.

523 The absolute dating of the Zutendaal gravels contributes to constrain the chronostratigraphical framework of the
524 Campine Plateau, and the Meuse River terraces. Several authors (e.g., Pannekoek, 1924; Paulissen, 1973) have
525 formulated the hypothesis that the Zutendaal gravels may represent the Main Terrace in the part of the Meuse
526 valley downstream of Maastricht. However, the correlation between terrace fragments located at different
527 locations along the Meuse River is still subject of scientific debate. However, it remains interesting to compare the
528 chronological framework of the Zutendaal gravels on top of the Campine Plateau with the Younger Main Terrace
529 levels of the Meuse River in the Liège area and the Ardennes. Van den Berg (1996) used paleomagnetic techniques
530 on the different sublevels of the Sint-Pietersberg Terrace to obtain age estimates of the Main Terrace in the region
531 of Maastricht. The age of the uppermost sublevel was estimated at 955 ka by Van den Berg (1996) and at 720 ka
532 by Van Balen et al. (2000) based on the same data. Both studies agree on an age of 650 ka for the next sublevel.

533 Rixhon et al. (2011) dated the Younger Main Terrace of the Meuse River in the locality of Romont, ~ 25 km
534 upstream of our sampling position, using in-situ produced ^{10}Be depth profiles. They obtained an age of 725 ± 120
535 ka (mean ± 1 SD). Although this age is somewhat older than the top of the Zutendaal gravels that we dated with
536 CRN depth modelling (i.e., 562_{-45}^{+211} , optimal solution with 95% CI), it is not inconsistent as it overlaps with the
537 CRN optimal solution considering the 95% confidence interval.

538

539 **5 Conclusion**

540 The aggradation and preservation mode of Middle Pleistocene braided river deposits was here studied based on in
541 situ cosmogenic radionuclide concentrations. To account for potential discontinuous aggradation, a numerical
542 model was developed to simulate the accumulation of cosmogenic radionuclides, ^{10}Be and ^{26}Al , in a sedimentary
543 sequence; and account for deposition and erosion phases and post-depositional exposure. The method was applied
544 to the Zutendaal gravels outcropping in NE Belgium, and 17 sediment samples were taken over a depth of 7 m and
545 processed for determination of ^{10}Be and ^{26}Al concentrations. The model parameters were optimized using reduced
546 chi square minimization. The Zutendaal gravels were deposited during (at least) three superimposed aggradational
547 phases that were interrupted by stability or erosion lasting ~40 kyr. This illustrates how long periods of non-
548 deposition alternate with rapid and short depositional events. The key chronostratigraphical outcomes of this study
549 based on the optimal model outcomes are: (1) the fluvial deposits found at 7 m depth in As are dated at 654_{-62}^{+218}
550 ka, thereby corresponding to MIS 16, (2) the uppermost sequence of these deposits is dated at 562_{-45}^{+211} ka,
551 corresponding to MIS 14, and thereby possibly deposited by another stream than the Meuse River that is assumed
552 to have shifted its course east by that time, and (3) the total formation time of the upper 7 m of the Zutendaal
553 gravels in As is about 90 kyr, so that the deposition of the entire gravel sheet could correspond to more than one
554 glacial period. The total formation time of the Zutendaal gravels constitutes nearly 20 % of the deposition age, and
555 shows the importance of considering the aggradation mode of braided rivers when applying CRN techniques to >
556 3 m deep sedimentary sequences.

557

558

559 **6 Acknowledgements**

560 NV acknowledges funding from a teaching assistantship provided by the Faculty of Sciences, UCLouvain, and FC
561 from the Fonds de la Recherche Scientifique (FRS-FNRS, Belgium). This study was undertaken in the framework
562 of Agreement CO-19-17-4420-00 between UCLouvain and SCK·CEN (Belgian Nuclear Research Centre). The
563 authors thank Marco Bravin for assistance with manipulation and processing samples in the ELIC laboratory.

564

565 **References**

- 566 Akçar, N., Ivy-Ochs, S., Alfimov, V., Schlunegger, F., Claude, A., Reber, R., Christl, M., Vockenhuber, C.,
567 Dehnert, A., Rahn, M., and Schlüchter, C.: Isochron-burial dating of glaciofluvial deposits: First results
568 from the Swiss Alps, *Earth Surf Process Landf* 42, 2414–2425, <https://doi.org/10.1002/esp.4201>, 2017.
- 569 Balco, G., Stone, J.O.H., and Mason, J.A.: Numerical ages for Plio-Pleistocene glacial sediment sequences by
570 $^{26}\text{Al}/^{10}\text{Be}$ dating of quartz in buried paleosols, *Earth & Planet. Sci. Lett.* 232, 179–191,
571 <https://doi.org/10.1016/j.epsl.2004.12.013>, 2005.
- 572 Balco, G., and Rovey, C.W.: An isochron method for cosmogenic-nuclide dating of buried soils and sediments,
573 *Am. J. Sci.* 308, 1083–1114, <https://doi.org/10.2475/10.2008.02>, 2008.
- 574 Bats, H., Paulissen, E., and Jacobs, P.: De grindgroeve Hermans te As. Een beschermd landschap, *Monumenten*
575 *en Landschappen* 14(2), 56-63, 1995.
- 576 Beerten, K., De Craen, M., and Wouters, L.: Patterns and estimates of post-Rupelian burial and erosion in the
577 Campine area, north-eastern Belgium, *Phys. Chem. Earth* 64, 12–20,
578 <https://doi.org/10.1016/j.pce.2013.04.003>, 2013.
- 579 Beerten, K., Heyvaert, V.M.A., Vandenberghe, D., Van Nieuland, J., and Bogemans, F., Revising the Gent
580 Formation: a new lithostratigraphy for Quaternary wind-dominated sand deposits in Belgium, *Geol. Belg.*
581 20 (1/2), 95–102, <https://doi.org/10.20341/gb.2017.006>, 2017.
- 582 Beerten, K., Dreesen, R., Janssen, J., and Van Uyten, D.: The Campine Plateau, in: *Landscapes and Landforms of*
583 *Belgium and Luxembourg*, edited by: Demoulin, A., Springer, Berlin, Germany, 193-
584 214, https://doi.org/10.1007/978-3-319-58239-9_12, 2018.
- 585 Braucher, R., del Castillo, P., Siame, L., Hidy, A.J., and Bourlés, D.L.: Determination of both exposure time and
586 erosion rate from an in situ-produced ^{10}Be depth profile: A mathematical proof of uniqueness. *Model*
587 *sensitivity and applications to natural cases*, *Quat. Geochronol.* 4, 56–67,
588 <https://doi.org/10.1016/j.quageo.2008.06.001>, 2009.
- 589 Braucher, R., Merchel, S., Borgomano, J., and Bourlès, D.L.: Production of cosmogenic radionuclides at great
590 depth: A multi element approach, *Earth & Planet. Sci Lett.* 309, 1–9,
591 <https://doi.org/10.1016/j.epsl.2011.06.036>, 2011.
- 592 Bristow, C.S., and Best, J.L.: Braided rivers: perspectives and problems, in: *Braided Rivers*, Geological Society
593 Special Publication No. 75, edited by: Best, J. L. and Bristow, C. S., Cambridge University Press,
594 London, UK, 1-H, <https://doi.org/10.1017/S001675680001253X>, 1993.
- 595 Busschers, F.S., Kasse, C., van Balen, R.T., Vandenberghe, J., Cohen, K.M., Weerts, H.J.T., Wallinga, J., Johns,
596 C., Cleveringa, P., and Bunnik, F.P.M.: Late Pleistocene evolution of the Rhine-Meuse system in the
597 southern North Sea basin: imprints of climate change, sea-level oscillation and glacio-isostasy, *Quat. Sci.*
598 *Rev.* 26, 3216–3248, <https://doi.org/10.1016/j.quascirev.2007.07.013>, 2007.
- 599 Chmeleff, J., von Blanckenburg, F., Kossert, K., and Jakob, D.: Determination of the ^{10}Be half-life by
600 multicollector ICP-MS and liquid scintillation counting, *Nucl. Instrum. Methods Phys. Res. B: Beam*
601 *Interact. Mater. At.* 268, 192–199, <https://doi.org/10.1016/j.nimb.2009.09.012>, 2010.
- 602 Christl, M., Vockenhuber, C., Kubik, P. W., Wacker, L., Lachner, J., Alfimov, V., and Synal, H. A.: The ETH
603 Zurich AMS facilities: Performance parameters and reference materials, *Nucl. Instrum. Methods Phys.*
604 *Res. B: Beam Interact. Mater. At.* 294, 29–38, <https://doi.org/10.1016/J.NIMB.2012.03.004>, 2013.

- 605 Claude, A., Akçar, N., Ivy-Ochs, S., Schlunegger, F., Kubik, P., Dehnert, A., Kuhlemann, J., Rahn, M., and
606 Schlüchter, C.: Timing of early Quaternary accumulation in the Swiss Alpine Foreland, *Geomorphology*
607 276, 71–85, <https://doi.org/10.1016/j.geomorph.2016.10.016>, 2017.
- 608 Cohen K.M., Gibbard, P.: *Global chronostratigraphical correlation table for the last 2.7 million years.*
609 *Subcommission on Quaternary Stratigraphy (International Commission on Stratigraphy)*, Cambridge,
610 *United Kingdom*, 2011.
- 611 Covault, J.A., Craddock, W.H., Romans, B.W., Fildani, A., and Gosai, M.: Spatial and temporal variations in
612 landscape evolution: Historic and longer-term sediment flux through global catchments, *J Geol* 121, 35–
613 56, <https://doi.org/10.1086/668680>, 2013.
- 614 De Brue, H., Poesen, J., and Notebaert, B.: What was the transport mode of large boulders in the Campine
615 Plateau and the lower Meuse valley during the mid-Pleistocene?, *Geomorphology* 228, 568–578,
616 <https://doi.org/10.1016/j.geomorph.2014.10.010>, 2015.
617
- 618 Dehnert, A., Kracht, O., Preusser, F., Akçar, N., Kemna, H.A., Kubik, P.W., and Schlüchter, C.: Cosmogenic
619 isotope burial dating of fluvial sediments from the Lower Rhine Embayment, Germany, *Quat. Geochronol.*
620 6, 313–325, <https://doi.org/10.1016/j.quageo.2011.03.005>, 2011.
- 621 Dehaen, E.: Unraveling the characteristics of the Early and Middle Pleistocene Meuse River: study of the
622 Zutendaal gravels on the Campine Plateau, MSc. thesis, Faculty of Sciences, UCLouvain, Belgium, 63 pp.,
623 2021.
- 624 Dunai, T.J. (Ed.): *Cosmogenic Nuclides*, Cambridge University Press, New York, USA,
625 <https://doi.org/10.1017/CBO9780511804519>, 2010.
- 626 Derese, C., Vandenberghe, D., Paulissen, E., and Van den haute, P.: Revisiting a type locality for Late Glacial
627 aeolian sand deposition in NW Europe: Optical dating of the dune complex at Opgrimbie (NE Belgium),
628 *Geomorphology* 109, 27–35, <https://doi.org/10.1016/j.geomorph.2008.08.022>, 2009.
- 629 Erlanger, E.D., Granger, D.E., and Gibbon, R.J.: Rock uplift rates in South Africa from isochron burial dating of
630 fluvial and marine terraces, *Geology* 40, 1019–1022, <https://doi.org/10.1130/G33172.1>, 2012.
- 631 Granger, D.E., and Muzikar, P.F.: Dating sediment burial with in situ-produced cosmogenic nuclides: theory,
632 techniques, and limitations, *Earth & Planet. Sci Lett.* 188, 269–281, [https://doi.org/10.1016/S0012-](https://doi.org/10.1016/S0012-821X(01)00309-0)
633 821X(01)00309-0, 2001.
- 634 Gullentops, F., Janssen, J., and Paulissen, E.: Saalian nivation activity in the Bosbeek valley, NE Belgium.
635 *Geologie en Mijnbouw* 72, 125–130, 1993.
- 636 Gullentops, F., Bogemans, F., de Moor, G., Paulissen, E., and Pissart, A.: Quaternary lithostratigraphic units
637 (Belgium), *Geol. Belg.* 4(1–2), 153–164, <https://doi.org/10.20341/gb.2014.051>, 2001.
- 638 Hancock, G.S., Anderson, R.S., Chadwick, O.A., and Finkel, R.C.: Dating fluvial terraces with ^{10}Be and ^{26}Al
639 profiles: application to the Wind River, Wyoming, *Geomorphology* 27, 41–60,
640 [https://doi.org/10.1016/S0169-555X\(98\)00089-0](https://doi.org/10.1016/S0169-555X(98)00089-0), 1999.
- 641 Hidy, A. J., Gosse, J. C., Pederson, J. L., Mattern, J. P., and Finkel, R. C.: A geologically constrained Monte
642 Carlo approach to modeling exposure ages from profiles of cosmogenic nuclides: An example from Lees
643 Ferry, Arizona, *Geom Geophys* 11(9), Q0AA10, <https://doi.org/10.1029/2010GC003084>, 2010.
- 644 Hidy, A.J., Gosse, J.C., Sanborn, P., and Froese, D.G.: Age-erosion constraints on an Early Pleistocene paleosol
645 in Yukon, Canada, with profiles of ^{10}Be and ^{26}Al : Evidence for a significant loess cover effect on
646 cosmogenic nuclide production rates, *Catena* 165, 260–271, <https://doi.org/10.1016/j.catena.2018.02.009>,
647 2018.

- 648 Knudsen, M.F., Egholm, D.L., and Jansen, J.D.: Time-integrating cosmogenic nuclide inventories under the
649 influence of variable erosion, exposure, and sediment mixing, *Quat. Geochronol.* 51, 110–119,
650 <https://doi.org/10.1016/j.quageo.2019.02.005>, 2019.
- 651 Korschinek, G., Bergmaier, A., Faestermann, T., Gerstmann, U.C., Knie, K., Rugel, G., Wallner, A., Dillmann,
652 I., Dollinger, G., Lierse Von Gostomski, C., Kossert, K., Maiti, M., Poutivtsev, M., and Rimmert, A.: A
653 new value for the half-life of ^{10}Be by Heavy-Ion Elastic Recoil Detection and liquid scintillation counting,
654 *Nucl. Instrum. Methods Phys. Res. B: Beam Interact. Mater. At.* 268, 187–191,
655 <https://doi.org/10.1016/j.nimb.2009.09.020>, 2010.
- 656
657 Lachner, J., Christl, M., Müller, A.M., Suter, M., and Synal, H.A.: ^{10}Be and ^{26}Al low-energy AMS using He-
658 stripping and background suppression via an absorber, *Nucl. Instrum. Methods Phys. Res. B: Beam*
659 *Interact. Mater. At.* 331, 209–214, <https://doi.org/10.1016/j.nimb.2013.11.034>, 2014.
- 660 Laloy, E., Beerten, K., Vanacker, V., Christl, M., Rogiers, B., and Wouters, L.: Bayesian inversion of a CRN
661 depth profile to infer Quaternary erosion of the northwestern Campine Plateau (NE Belgium), *Earth Surf.*
662 *Dyn.* 5, 331–345, <https://doi.org/10.5194/esurf-5-331-2017>, 2017.
- 663 Lauer, T., Frechen, M., Hoselmann, C., and Tsukamoto, S.: Fluvial aggradation phases in the Upper Rhine
664 Graben-new insights by quartz OSL dating, *Proc Geol Assoc* 121, 154–161,
665 <https://doi.org/10.1016/j.pgeola.2009.10.006>, 2010.
- 666 Lauer, T., Weiss, M., Bernhardt, W., Heinrich, S., Rappsilber, I., Stahlschmidt, M.C., Suchodoletz, H. von, and
667 Wansa, S.: The Middle Pleistocene fluvial sequence at Uichteritz, central Germany: Chronological
668 framework, paleoenvironmental history and early human presence during MIS 11, *Geomorphology* 354,
669 107016, <https://doi.org/10.1016/j.geomorph.2019.107016>, 2020.
- 670 Le Dortz, K. le, Meyer, B., Sébrier, M., Braucher, R., Nazari, H., Benedetti, L., Fattahi, M., Bourlès, D.,
671 Foroutan, M., Siame, L., Rashidi, A., and Bateman, M.D.: Dating inset terraces and offset fans along the
672 Dehshir Fault (Iran) combining cosmogenic and OSL methods, *Geophys. J. Int.* 185, 1147–1174,
673 <https://doi.org/10.1111/j.1365-246X.2011.05010.x>, 2011.
- 674 Margreth, A., Gosse, J.C., and Dyke, A.S.: Quantification of subaerial and episodic subglacial erosion rates on
675 high latitude upland plateaus: Cumberland Peninsula, Baffin Island, Arctic Canada, *Quat. Sci. Rev.* 133,
676 108–129, <https://doi.org/10.1016/j.quascirev.2015.12.017>, 2016.
- 677 Martin, L.C.P., Blard, P.H., Balco, G., Lavé, J., Delunel, R., Lifton, N., and Laurent, V.: The CREP program and
678 the ICE-D production rate calibration database: A fully parameterizable and updated online tool to
679 compute cosmic-ray exposure ages, *Quat. Geochronol.* 38, 25–49,
680 <https://doi.org/doi:10.1016/j.quageo.2016.11.006>, 2017.
- 681 Miall, A.D. (Ed.): *The Geology of fluvial deposits*, Springer, Berlin, Germany, [https://doi.org/10.1007/978-3-](https://doi.org/10.1007/978-3-662-03237-4)
682 [662-03237-4](https://doi.org/10.1007/978-3-662-03237-4), 1996.
- 683 Mol, J., Vandenberghe, J., and Kasse, C.: River response to variations of periglacial climate in mid-latitude
684 Europe, *Geomorphology*, 33(3–4), 131–148, [https://doi.org/10.1016/S0169-555X\(99\)00126-9](https://doi.org/10.1016/S0169-555X(99)00126-9), 2000.
- 685 Nichols, K. K., Bierman, P. R., Hooke, R. L., Clapp, E. M., and Caffee, M.: Quantifying sediment transport on
686 desert piedmonts using ^{10}Be and ^{26}Al , *Geomorphology*, 45, 105–125, www.elsevier.com/locate/geomorph,
687 2002.
- 688 Nichols, K. K., Bierman, P. R., Eppes, M. C., Caffee, M., Finkel, R., and Larsen, J.: Late Quaternary history of
689 the Chemehuevi Mountain Piedmont, Mojave Desert, deciphered using ^{10}Be and ^{26}Al , *American Journal of*
690 *Science*, 305(5), 345–368, <https://doi.org/10.2475/ajs.305.5.345>, 2005.

691

- 692 Nishiizumi, K.: Cosmic ray production rates of ^{10}Be and ^{26}Al in quartz from glacially polished rocks, *J. Geophys.*
693 *Res. Solid Earth* 94, 17907-17915, <https://doi.org/10.1029/jb094ib12p17907>, 1989.
- 694 Nishiizumi, K.: Preparation of ^{26}Al AMS standards, *J Nucl. Instrum. Methods Phys. Res. B: Beam Interact.*
695 *Mater. At.* 223-224, 388-392, <https://doi.org/10.1016/j.nimb.2004.04.075>, 2004.
- 696 Pannekoek, A.J.: Einigen Notizen über die Terrassen in Mittel- und Nord-Limburg. *Natuurhistorisch Maandblad*
697 *13*, 89-92, 1924.
- 698 Paulissen, E.: De Morfologie en de Kwartairstratigrafie van de Maasvallei in Belgisch Limburg, *Verhandelingen*
699 *van de koninklijke Vlaamse academie voor wetenschappen, letteren en schone kunsten van België, Klasse*
700 *der Wetenschappen* 127, 1-266, 1973.
- 701 Paulissen, E.: Les nappes alluviales et les failles Quaternaires du Plateau de Campine, in: *Guides Géologiques*
702 *Régionaux – Belgique*, edited by : Robaszynski, F., and Dupuis, C., Masson, Paris, France, 167-
703 170, 1983.
- 704
705 Portenga, E.W., and Bierman, P.R.: Understanding earth's eroding surface with ^{10}Be , *GSA Today* 21, 4-10,
706 <https://doi.org/10.1130/G111A.1>, 2011.
- 707 Rixhon, G., Braucher, R., Bourlès, D., Siame, L., Bovy, B., and Demoulin, A.: Quaternary river incision in NE
708 Ardennes (Belgium)-Insights from $^{10}\text{Be}/^{26}\text{Al}$ dating of river terraces, *Quat. Geochronol.* 6, 273-284,
709 <https://doi.org/10.1016/j.quageo.2010.11.001>, 2011.
- 710 Rixhon, G., Bourlès, D.L., Braucher, R., Siame, L., Cordy, J.M., and Demoulin, A.: ^{10}Be dating of the Main
711 Terrace level in the Amblève valley (Ardennes, Belgium): New age constraint on the archaeological and
712 palaeontological filling of the Belle-Roche palaeokarst, *Boreas* 43, 528-542,
713 <https://doi.org/10.1111/bor.12066>, 2014.
- 714 Rizza, M., Abdrakhmatov, K., Walker, R., Braucher, R., Guillou, V., Carr, A.S., Campbell, G., McKenzie, D.,
715 Jackson, J., Aumaître, G., Bourlès, D.L., and Keddadouche, K.: Rate of slip from multiple Quaternary
716 dating methods and paleoseismic investigations along the Talas-Fergana Fault: tectonic implications for
717 the Tien Shan Range, *Tectonics* 38, 2477-2505, <https://doi.org/10.1029/2018TC005188>, 2019.
- 718 Rodés, A., Pallàs, R., Braucher, R., Moreno, X., Masana, E., and Bourlès, D.: Effect of density uncertainties in
719 cosmogenic ^{10}Be depth-profiles: Dating a cemented Pleistocene alluvial fan (Carboneras Fault, SE Iberia),
720 *Quat. Geochronol.* 6, 186-194, <https://doi.org/10.1016/j.quageo.2010.10.004>, 2011.
- 721 Schaller, M., von Blanckenburg, F., Hovius, N., and Kubik, P.W.: Large-scale erosion rates from in situ-
722 produced cosmogenic nuclides in European river sediments, *Earth & Planet. Sci Lett.* 188, 441-458,
723 [https://doi.org/10.1016/S0012-821X\(01\)00320-X](https://doi.org/10.1016/S0012-821X(01)00320-X), 2001.
- 724 Schaller, M., Ehlers, T. A., Blum, J.D., and Kallenberg, M. A.: Quantifying glacial moraine age, denudation, and
725 soil mixing with cosmogenic nuclide depth profiles, *J. Geophys. Res.* 114, F01012,
726 <https://doi.org/10.1029/2007JF000921>, 2009.
- 727 Schoonejans, J., Vanacker, V., Opfergelt, S., Granet, M., and Chabaux, F.: Coupling uranium series and ^{10}Be
728 cosmogenic radionuclides to evaluate steady-state soil thickness in the Betic Cordillera, *Chem. Geol.* 446,
729 99-109, <https://doi.org/10.1016/J.CHEMGEO.2016.03.030>, 2016.
- 730
731 Siame, L., Bellier, O., Braucher, R., Sébrier, M., Cushing, M., Bourlès, D., Hamelin, B., Baroux, E., Voogd, B.
732 de, Raisbeck, G., and Yiou, F.: Local erosion rates versus active tectonics: Cosmic ray exposure modelling
733 in Provence (south-east France), *Earth & Planet. Sci Lett.* 220, 345-364, [https://doi.org/10.1016/S0012-821X\(04\)00061-5](https://doi.org/10.1016/S0012-821X(04)00061-5), 2004.
- 734

- 735 Sougnez, N., and Vanacker, V.: The topographic signature of Quaternary uplift in the Ardennes massif (Western
736 Europe), *Hydrol Earth Syst Sci* 15, 1095-1107, <https://doi.org/10.5194/hess-15-1095-2011>, 2011.
- 737 Stone, J.O.: Air pressure and cosmogenic isotope production, *J. Geophys. Res. Solid Earth* 105, 23753–23759,
738 <https://doi.org/10.1029/2000jb900181>, 2000.
- 739 Taylor, J.R. (Ed.): An introduction to error analysis, University science books, Sausalito, California, USA, 1997.
- 740 Vanacker, V., von Blanckenburg, F., Hewawasam, T., and Kubik, P.W.: Constraining landscape development of
741 the Sri Lankan escarpment with cosmogenic nuclides in river sediment, *Earth & Planet. Sci Lett.* 253, 402–
742 414, <https://doi.org/10.1016/j.epsl.2006.11.003>, 2007.
- 743 Vanacker V., von Blanckenburg F., Govers G., Molina A., Campforts B., and Kubik P.W.: Transient river
744 response, captured by channel steepness and its concavity, *Geomorphology* 228, 234 – 243,
745 <https://doi.org/10.1016/j.geomorph.2014.09.013>, 2015.
- 746 Van Balen, R.T., Houtgast, R.F., van der Wateren, F.M., Vandenberghe, J., and Bogaart, P.W.: Sediment budget
747 and tectonic evolution of the Meuse catchment in the Ardennes and the Roer Valley Rift System, *Glob.*
748 *Planet* 27, 113-129, [https://doi.org/10.1016/S0921-8181\(01\)00062-5](https://doi.org/10.1016/S0921-8181(01)00062-5), 2000.
- 749 van den Berg, M.: Fluvial sequences of the Meuse-a 10 Ma record of neotectonics and climate change at various
750 time-scales, PhD thesis, Wageningen University, 181 pp., 1996.
- 751
752
- 753 Vandenberghe, J.: Timescale, Climate and River Development, *Quat. Sci. Rev.* 14, 631-
754 639, [https://doi.org/0277-3791\(95\)00043-7](https://doi.org/0277-3791(95)00043-7), 1995.
- 755 Vandenberghe, J.: A typology of Pleistocene cold-based rivers, *Quat. Int.* 79, 111-121, [https://doi.org/1040-6182/01/\\$20.00](https://doi.org/1040-6182/01/$20.00), 2001.
- 756
- 757 Vandenberghe, D., Vanneste, K., Verbeeck, K., Paulissen, E., Buylaert, J.-P., De Corte, F. and Van den haute,
758 P.: Late Weichselian and Holocene earthquake events along the Geleen fault in NE Belgium: OSL age
759 constraints, *Quaternary International*, 199, 56–74, <https://doi.org/10.1016/j.quaint.2007.11.017>, 2009.
- 760 Vandenberghe, J.: River terraces as a response to climatic forcing: Formation processes, sedimentary
761 characteristics and sites for human occupation, *Quat. Int.* 370, 3–11,
762 <https://doi.org/10.1016/j.quaint.2014.05.046>, 2015.
- 763 Vandermaelen, N., Vanacker, V., Clapuyt, F., Christl, M., and Beerten, K.: Reconstructing the depositional
764 history of Pleistocene fluvial deposits based on grain size, elemental geochemistry and in situ ¹⁰Be data,
765 *Geomorphology* 402, 108127, <https://doi.org/10.1016/j.geomorph.2022.108127>, 2022.
- 766 Vanneste, K., Verbeeck, K., Camelbeeck, T., Paulissen, E., Meghraoui, M., Renardy, F., Jongmans, D., and
767 Frechen, M.: Surface-rupturing history of the Bree fault scarp, Roer Valley graben: Evidence for six events
768 since the late Pleistocene, *J. Seismol.* 5, 329–359, 2001.
- 769 von Blanckenburg, F., Belshaw, N.S., and O’Nions, R.K.: Separation of ⁹Be and cosmogenic ¹⁰Be from
770 environmental materials and SIMS isotope dilution analysis, *Chem. Geol.* 129, 93–99,
771 [https://doi.org/10.1016/0009-2541\(95\)00157-3](https://doi.org/10.1016/0009-2541(95)00157-3), 1996.
- 772 Westerhoff, W.E., Kemna, H.A., and Boenigk, W.: The confluence area of Rhine, Meuse, and Belgian rivers:
773 Late Pliocene and Early Pleistocene fluvial history of the northern Lower Rhine Embayment, *NETH J*
774 *GEOSCI* 87, 107–125, <https://doi.org/10.1017/S0016774600024070>, 2008.

775 Xu, L., Ran, Y., Liu, H., and Li, A.: ^{10}Be -derived sub-Milankovitch chronology of Late Pleistocene alluvial
776 terraces along the piedmont of SW Tian Shan, *Geomorphology* 328, 173–182,
777 <https://doi.org/10.1016/j.geomorph.2018.12.009>, 2019.